Research Square

Preprints are preliminary reports that have not undergone peer review.
They should not be considered conclusive, used to inform clinical practice,
or referenced by the media as validated information.

High-Cycle Fatigue Behavior and Fatigue Crack Growth at 450 °C in a Dissimilar 2.25Cr/Modified FB2 Welded Rotor Joint

Feipeng Yang

156098031@qq.com

Harbin Turbine Company Limited

Ruihang Liu

Harbin Turbine Company Limited

Lingjian Meng

China Productivity Center For Machinery

Zhicheng Su

Harbin Turbine Company Limited

Bo Wang

Harbin Welding Institute Limited Company of China Academy of Machinery Science and Technology Group

Yan Du

China Productivity Center For Machinery

Research Article

Keywords: welded rotor, high-cycle fatigue, mean stress, fatigue crack growth, stress ratio

Posted Date: November 18th, 2026

DOI: https://doi.org/10.21203/rs.3.rs-11386290/v1

License: This work is licensed under a Creative Commons Attribution 4.0 International License.
Read Full License

Additional Declarations: No competing interests reported.

High-Cycle Fatigue Behavior and Fatigue Crack Growth at 450 °C in a Dissimilar 2.25Cr/Modified FB2 Welded Rotor Joint

Abstract

High-cycle fatigue (HCF) and fatigue crack growth (FCG) were investigated in a dissimilar 2.25Cr (10325MTE)/modified FB2 (MTR10A) welded rotor joint. Room-temperature HCF tests were performed at stress ratios R = −1, −0.5, and 0.1, followed by scanning electron microscopy and energy-dispersive X-ray spectroscopy of selected fracture surfaces. FCG tests at 450 °C covered the root weld metal, near-outer-surface weld metal, and both heat-affected zones at R = 0.1, 0.4, and 0.7. The conditional fatigue strengths at 10^7 cycles, expressed as maximum stress, were 300, 383, and 550 MPa, respectively, corresponding to stress amplitudes of 300.0, 287.5, and 247.5 MPa. The decreasing allowable stress amplitude was associated with increasing tensile mean stress. Fatigue striations and localized quasi-cleavage-like features occurred in stable propagation regions, while dimples predominated in final fracture regions. Initiation sites included surface discontinuities and regions adjacent to subsurface particles. Paris relationships described stable FCG in all 24 compact-tension specimens. At ΔK = 20 MPa·m$^{1/2}$ and R = 0.1, mean fitted FCG rates were 3.54×10^{-5} and 5.68×10^{-5} mm/cycle in the left and right heat-affected zones, respectively. For the root weld metal, the mean fitted rate at R = 0.4 (1.16×10^{-4} mm/cycle) exceeded that at R = 0.7 (9.34×10^{-5} mm/cycle). The FCG response depended on joint region and stress ratio, with different levels of scatter between paired specimens.

Keywords: welded rotor; high-cycle fatigue; mean stress; fatigue crack growth; stress ratio

1. Introduction

Large welded steam-turbine rotors experience cyclic mechanical loading and elevated temperatures in service. The fatigue performance of their welded joints is closely linked to rotor structural integrity. Using dissimilar heat-resistant steels allows different parts of a rotor to meet distinct property requirements, but variations in microstructure and mechanical properties among the weld metal, heat-affected zones (HAZs), and base metals produce a heterogeneous fatigue response. Wang et al. [1] investigated the HCF behavior of a dissimilar-metal welded joint for an ultra-supercritical steam-turbine rotor and subsequently examined fracture characteristics in CrMoV/NiCrMoV rotor welds [2]. Deng et al. [3] reported differences in FCG behavior among regions of a dissimilar 9Cr/CrMoV welded joint. These studies show that fatigue assessment of welded joints encompasses both overall cyclic load-bearing capacity and crack propagation in individual joint regions.

In HCF testing, the stress ratio R governs the relationship among maximum stress, stress amplitude, and mean stress. As R changes, S–N curves expressed in terms of maximum stress may show trends unlike those obtained using stress amplitude. Wang et al. [4] investigated HCF life and fracture behavior of 9%Cr rotor steel at 630 °C under different stress ratios and established the influence of mean stress. For this dissimilar-steel joint, the S–N relationships at different stress ratios are considered alongside constant-life stress-amplitude–mean-stress relationships and characteristic crack initiation sites identified by fractography.

FCG behavior varies with the weld region and stress ratio. Deng et al. [3] compared crack growth in the base metals, weld metal, and HAZs of a dissimilar-steel joint. Sun et al. [5] examined near-threshold FCG in martensitic heat-resistant steel welds exposed to high-temperature air, and later examined the near-threshold response of the weld metal and HAZ in an ex-service CrMoV steel joint [6]. Together, these investigations highlight the relevance of weld-region heterogeneity and stress ratio across different materials and crack-growth regimes. For the Paris-regime behavior at 450 °C considered here, comparison of FCG rates at a common stress-intensity-factor range, ΔK, provides a basis for identifying region-dependent responses.

In the Paris regime, the fatigue crack growth rate, da/dN, is usually represented by a power-law function of ΔK. Both the Paris coefficient C and exponent m influence the position and slope of the growth-rate curve; neither parameter alone determines the FCG rate at a specified ΔK. Duplicate specimens from the same weld region may also exhibit different growth rates, making comparisons of individual fits and paired specimens important. The stress-ratio correction proposed by Walker [7] provides an empirical approach for representing FCG data obtained at multiple stress ratios within a unified relationship.

A total of 78 cylindrical specimens from a dissimilar 2.25Cr/modified FB2 welded rotor joint underwent room-temperature HCF testing at R = −1, −0.5, and 0.1. The measurements were used to assess S–N behavior and mean-stress effects, together with representative fracture morphologies. FCG tests at 450 °C were also conducted on 24 compact-tension (CT) specimens from the root weld metal, near-outer-surface weld metal, and both HAZs at R = 0.1, 0.4, and 0.7. Individual Paris relationships, fixed-ΔK rate comparisons, and combined Walker fits were examined to evaluate variations with location and stress ratio.

2. Materials and Experimental Methods

2.1. Welded Rotor Joint and Specimen Locations

The material was an annular simulated joint made from dissimilar 2.25Cr (10325MTE) and modified FB2 (MTR10A) steels for a 630 °C-class welded rotor. TG-S9Cb filler wire with a diameter of 1.2 mm was used. The material was sectioned by band sawing followed by wire electrical discharge machining. FCG specimens were taken from the root weld metal (GH), near-outer-surface weld metal (WH), and the left and right near-outer-surface HAZs (WL and WR, respectively). The WL region is adjacent to the 2.25Cr base metal, whereas the WR region is adjacent to modified FB2. Cylindrical specimens with a diameter of 10 mm were extracted from the near-outer-surface welded-joint region for room-temperature HCF tests; CT specimens were used for FCG tests.

2.2. High-Cycle Fatigue Tests

Room-temperature HCF tests were performed in accordance with GB/T 3075–2021 [8] using a QBG-100 high-frequency fatigue testing machine and cylindrical specimens 10 mm in diameter. Sinusoidal loading at 130–140 Hz was applied at R = −1, −0.5, and 0.1, with a run-out criterion of 10^7 cycles. Specimen groups were used to obtain finite-life S–N data, and the staircase method was used to estimate the conditional fatigue strength at 10^7 cycles. A total of 78 specimens were tested: 27 at R = −1, 27 at R = −0.5, and 24 at R = 0.1. 18 of these specimens reached 10^7 cycles without failure.

2.3. Fatigue Crack Growth Tests at 450 °C

FCG testing at 450 °C was performed in accordance with GB/T 6398–2017 [9]. The CT specimens had a nominal width W of about 50 mm and a thickness B of approximately 10 mm. The machined notch length was approximately 9.0–9.2 mm, and the crack length after fatigue precracking was approximately 12.0 mm. Sinusoidal loading at constant load amplitude with increasing K was applied at R = 0.1, 0.4, and 0.7. Crack length was monitored using the electrical potential-drop method. Two CT specimens represented each combination of the four joint regions and three stress ratios, giving 24 specimens overall. Specimen identifiers and individual Paris-fit parameters are listed in Table 5.

2.4. Data Reduction and Models

The cyclic stress amplitude, σa, and mean stress, σm, were calculated from the maximum stress, σmax, and stress ratio R as follows:

$$\sigma a = \sigma max(1 - R)/2 \quad (1)$$

$$\sigma m = \sigma max(1 + R)/2 \quad (2)$$

The room-temperature HCF results were fitted with an empirical three-parameter S–N relationship containing an asymptotic term. Conditional fatigue strengths at 10^7 cycles came from the staircase tests, whereas constant-life stress combinations were calculated from the corresponding fitted S–N equations. Specimens that did not fail by the run-out criterion were identified as run-outs in the plots; the 10^7-cycle fatigue strength was reported as a test-based measure at the specified cycle limit.

Stable crack-growth data at 450 °C were described using the Paris relationship:

$$da/dN = C(\Delta K)^m \quad (3)$$

The FCG rate da/dN is given in mm/cycle, with ΔK in MPa·$m^{1/2}$. Values of ΔK = 20 and 25 MPa·$m^{1/2}$ were selected within the common fitted intervals for each comparison. At both ΔK levels, rates were calculated separately from the fits of two independent CT specimens; their arithmetic mean represented each region–stress-ratio

combination. The difference between the paired rates was quantified as $D = 2|v_1 - v_2|/(v_1 + v_2) \times 100\%$, where v_1 and v_2 denote the fitted FCG rates at the same ΔK.

Combined fits across stress ratios were compared using ΔK, $K_{max} = \Delta K/(1 - R)$, and the Walker equivalent driving force:

$$da/dN = C[\Delta K/(1 - R)^{(1 - \gamma)}]^m \quad (4)$$

Walker parameters were fitted to the multi-stress-ratio FCG data for each region at 450 °C. The coefficients of determination, R^2, evaluated for the same datasets were used to compare the goodness of fit of the three driving-force formulations.

2.5. SEM and EDS Examination of HCF Fracture Surfaces

Representative HCF fracture surfaces were selected at R = −1, −0.5, and 0.1, covering lives of approximately 10^5, 3×10^5, and 6.5×10^6–7.7×10^6 cycles. Scanning electron microscopy was used to examine initiation sites, stable propagation regions, and final fracture surfaces. Local compositions of particles and deposits adjacent to initiation sites were analyzed by EDS.

AI-assisted manuscript preparation. An AI-based language model was used during manuscript preparation to assist with translation, language editing, and drafting of text based on author-provided experimental materials. The authors retain responsibility for verifying all research data, analyses, interpretations, and the final manuscript.

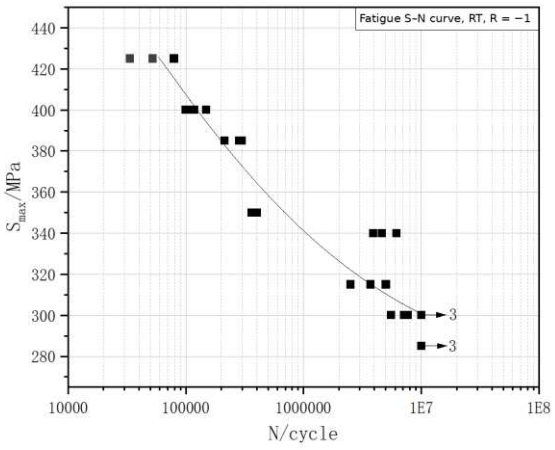
Table 1. Summary of fatigue test conditions

Item	High-cycle fatigue	Fatigue crack growth
Temperature	Room temperature	450 ℃
Specimen	Ø10 mm cylindrical specimen	CT specimen, W ≈ 50 mm, B ≈ 10 mm
Stress ratio R	−1, −0.5, 0.1	0.1, 0.4, 0.7
Waveform	Sinusoidal	Sinusoidal
Test mode/output	Run-outs at 10^7 cycles; S–N relation	Increasing K under constant load amplitude; da/dN–ΔK relation
Standard	GB/T 3075—2021	GB/T 6398—2017
Number of specimens	R = −1: 27; R = −0.5: 27; R = 0.1: 24	2 per region × R; 24 total

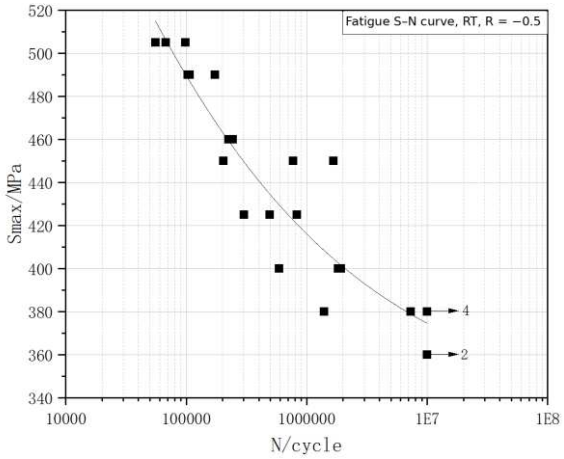
3. Results

3.1. High-Cycle Fatigue Behavior at Different Stress Ratios

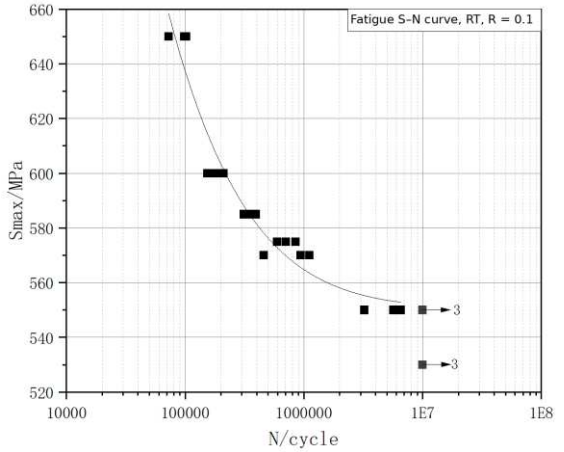
The room-temperature S–N curves at R = −1, −0.5, and 0.1 appear in Fig. 1. For all three groups, fatigue life increased overall with decreasing maximum stress, and six specimens per group remained unbroken at the 10^7-cycle limit. The three-parameter S–N fits yielded coefficients of determination of 0.936, 0.973, and 0.978, respectively (Table 2), indicating distinct stress–life relationships at the three stress ratios.



(a) R = −1



(b) R = −0.5



(c) R = 0.1

Fig. 1 S–N curves of the welded rotor joint at different stress ratios

Staircase testing yielded conditional fatigue strengths at 10^7 cycles, expressed as maximum stress, of 300, 383.33, and 550 MPa for R = −1, −0.5, and 0.1, respectively (Table 2). Although this maximum-stress-based strength increased with R, the opposite trend appeared when the load levels were converted to cyclic stress amplitudes, reflecting the different combinations of load amplitude and mean stress.

Table 2. High-cycle fatigue parameters at different stress ratios

Stress ratio R	Fitted S–N equation	10^7-cycle strength (MPa)	R^2
-1	lgN=9.67-2.17lg(Smax-284.5)	300	0.936
-0.5	lgN=8.04-1.42 lg(Smax-379.9)	383	0.973
0.1	lgN=7.94-1.56lg(Smax-550)	550	0.978

Note: σa and σm were calculated from the corresponding 10^7-cycle conditional fatigue strengths and nominal stress ratios.

3.2. Effect of Mean Stress on High-Cycle Fatigue Behavior

Maximum stresses recorded at different R values were converted to stress amplitudes, σa, and mean stresses, σm, using Eqs. (1) and (2). Constant-life stress combinations at 10^5, 10^6, and 10^7 cycles were then obtained from the fitted S–N relationships. Figure 2 and Table 3 present the resulting σa–σm relationships.

At 10^7 cycles, the conditional fatigue strengths corresponded to (σm, σa) pairs of (0, 300.0), (95.8, 287.5), and (302.5, 247.5) MPa. The conditional fatigue stress amplitude consequently fell from 300.0 to 247.5 MPa, a decrease of 17.5%, as tensile mean stress rose from 0 to 302.5 MPa.

A decrease in stress amplitude with increasing tensile mean stress was also evident at the other two constant-life levels (Table 3). At 10^5 cycles, σa decreased from 426.4 to 282.0 MPa as R increased from −1 to 0.1; at 10^6 cycles, it decreased from 333.6 to 255.4 MPa. These consistent trends demonstrate a pronounced influence of tensile mean stress on the room-temperature HCF load-bearing capacity of the welded joint across the investigated life range.

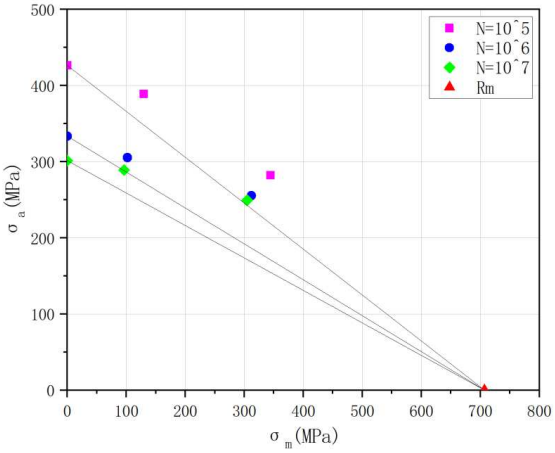


Fig. 2 Constant-life diagrams at room temperature

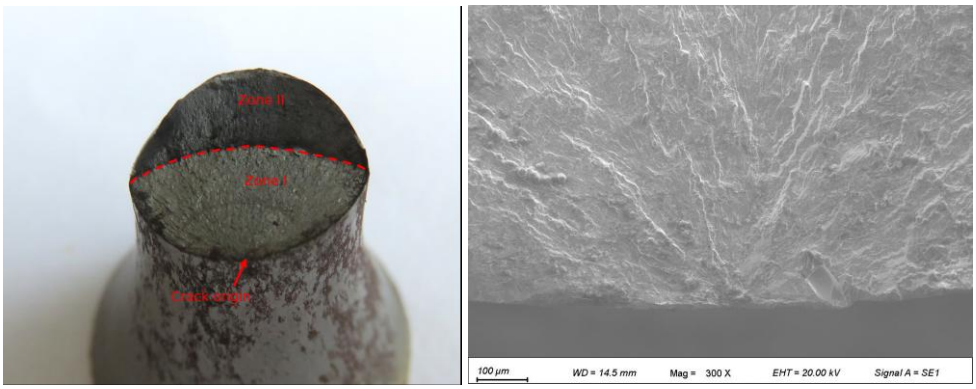
Table 3. Stress amplitudes and mean stresses at different fatigue lives and stress ratios

	N = 10^5 cycles		**N = 10^6 cycles**		**N = 10^7 cycles**	
R	σa (MPa)	σm (MPa)	σa (MPa)	σm (MPa)	σa (MPa)	σm (MPa)
-1	426.4	0.0	333.6	0.0	301.5	0.0
-0.5	388.7	129.6	305.4	101.8	289.0	96.3
0.1	282.0	344.7	255.4	312.1	249.3	304.7

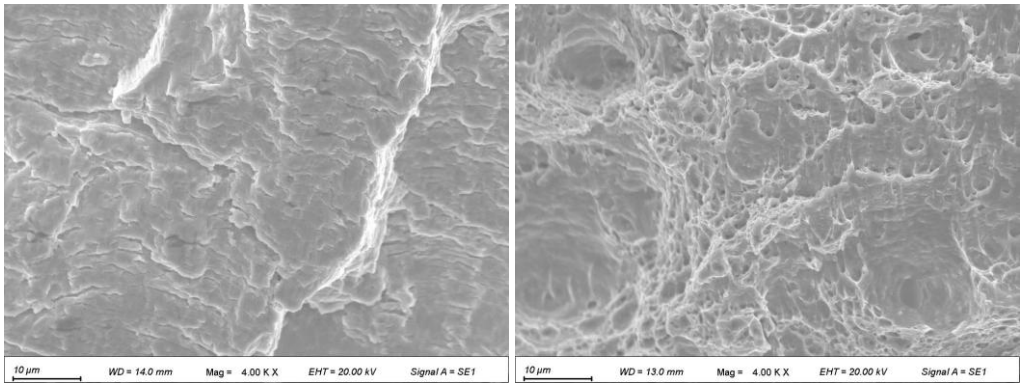
3.3. HCF Fractography and Crack Initiation Characteristics

Figures 3–5 depict the fracture surfaces of representative short-life specimens tested at the three stress ratios. At R = −1 and R = −0.5, the macroscopic fracture surfaces were characterized by relatively flat stable crack-growth regions and final fracture regions located opposite the initiation sites. The initiation site of the R = −1 specimen was near the subsurface (Fig. 3b); at R = −0.5, initiation was associated with a subsurface cavity and adjacent particles (Fig. 4b,c). Local EDS analysis revealed oxygen and aluminum mass fractions of 47.45% and 46.30%, respectively, together with minor amounts of Fe, Si, and Mg (Table 4), indicative of an Al–O-rich particle. Fatigue striations and localized quasi-cleavage-like features were observed in the stable propagation regions (Figs. 3c and 4d), whereas dimples predominated in the final fracture regions (Figs. 3d and 4e). The short-life specimen tested at R = 0.1 exhibited multiple surface initiation sites (Fig. 5), with characteristic fatigue propagation and ductile final-fracture features.

Figures 6–8 illustrate the fracture surfaces of representative longer-life specimens. Crack initiation occurred near the interior of the fracture surface for the R = −1 specimen and near the surface for the R = −0.5 and 0.1 specimens. Fatigue striations were identified in the stable crack-growth regions of all three specimens, while the final fracture regions were predominantly dimpled. The combined observations indicate that local discontinuities at both surface and subsurface locations can act as fatigue crack initiation sites.

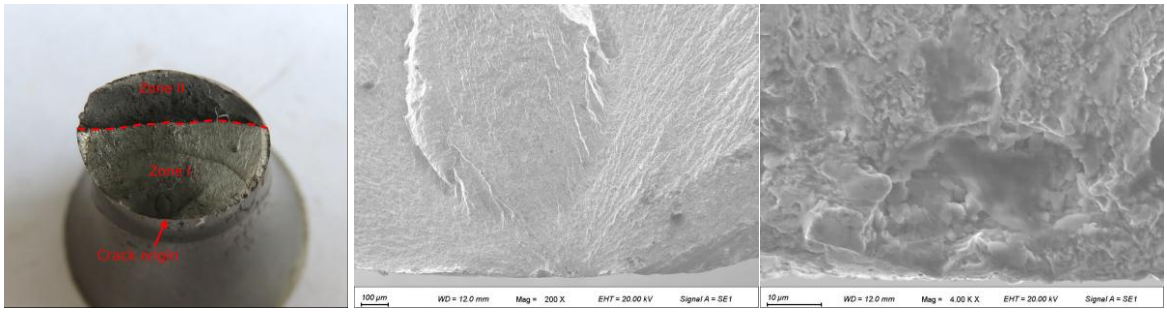


(a) Overall fracture surface (b) Crack initiation site

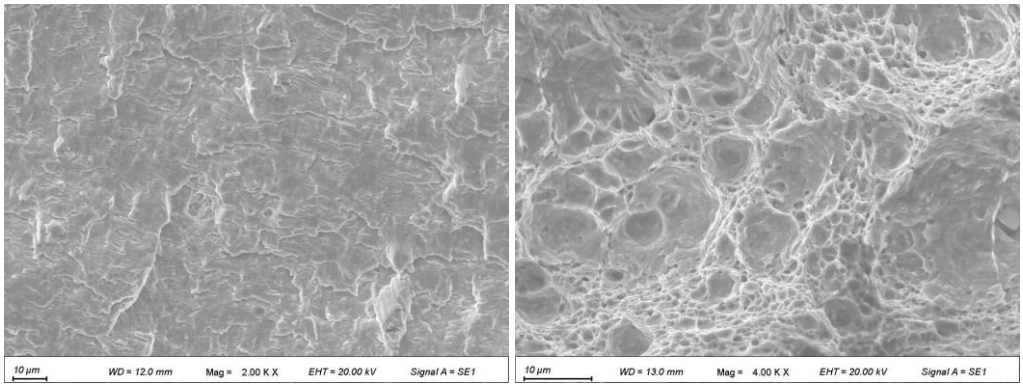


(c) Crack propagation region (d) Final fracture region

Fig. 3 Fracture morphology of a short-life HCF specimen at R = −1



(a) Overall fracture surface (b) Initiation site (c) Enlarged initiation site

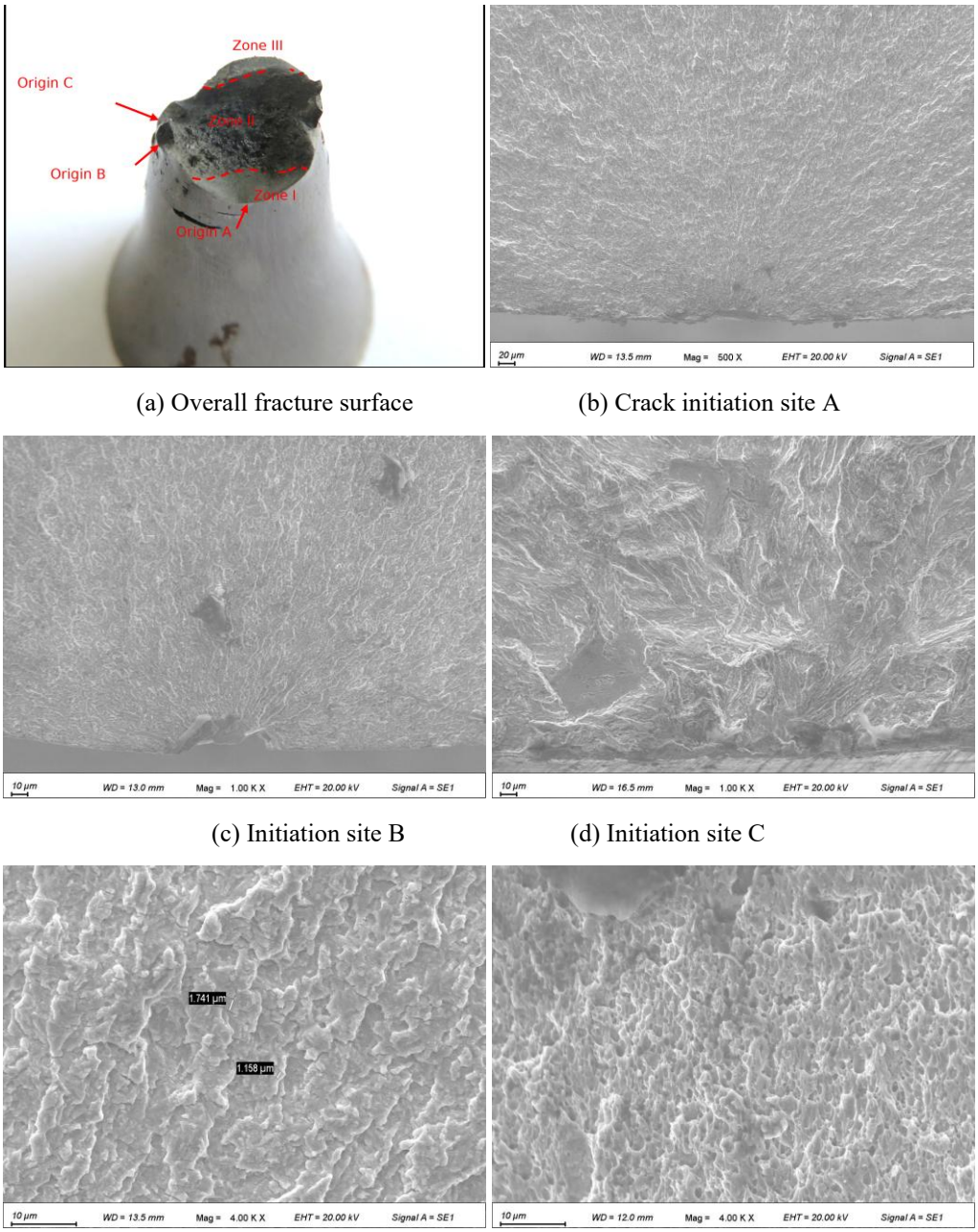


(d) Crack propagation region (e) Final fracture region

Fig. 4 Fracture morphology of a short-life HCF specimen at R = −0.5

Table 4. EDS elemental mass fractions of a particle adjacent to a representative crack initiation site

Element	Si	Fe	O	Mg	Al
Mass fraction (%)	2.30	3.05	47.45	0.90	46.30

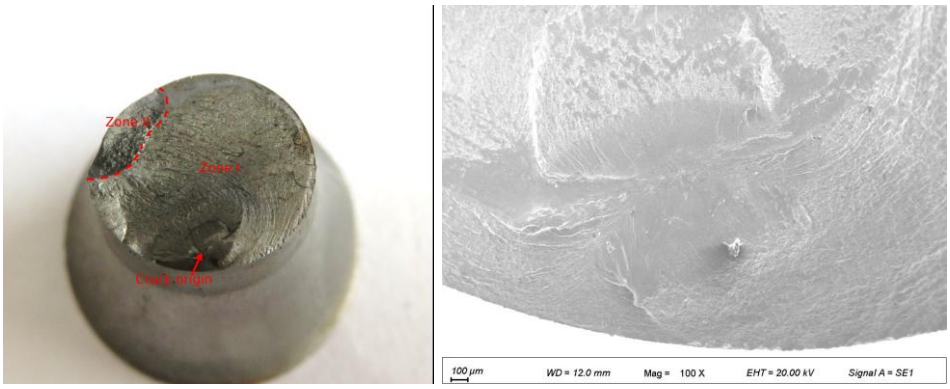


(a) Overall fracture surface (b) Crack initiation site A

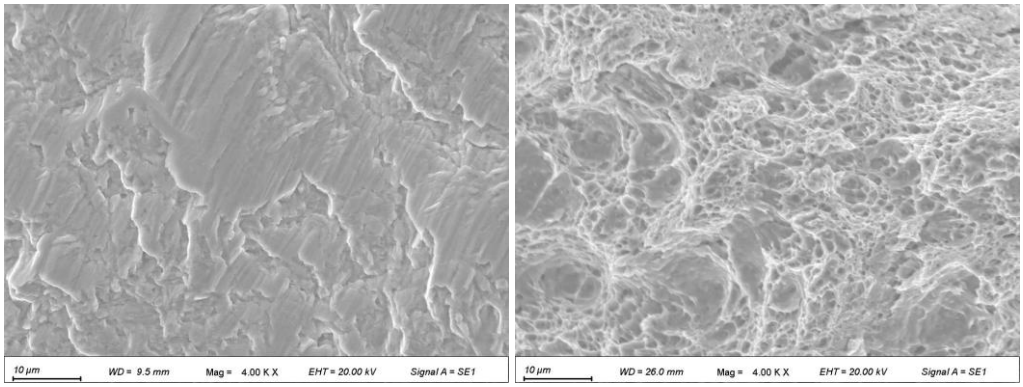
(c) Initiation site B (d) Initiation site C

(e) Crack propagation region (f) Final fracture region

Fig. 5 Fracture morphology of a short-life HCF specimen at R = 0.1

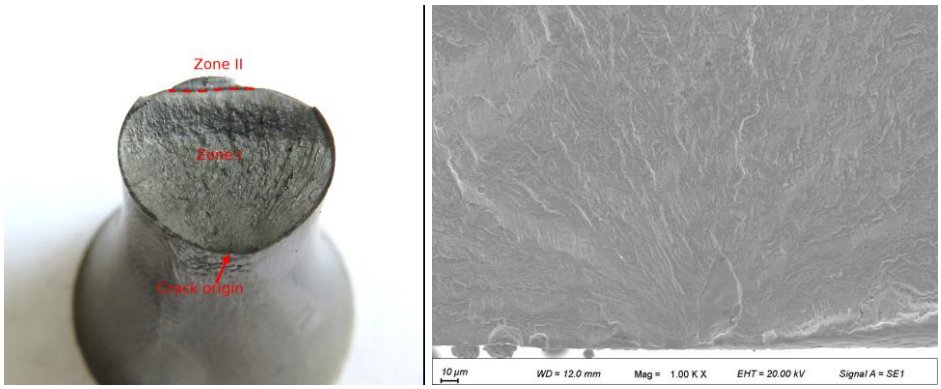


(a) Overall fracture surface (b) Crack initiation site

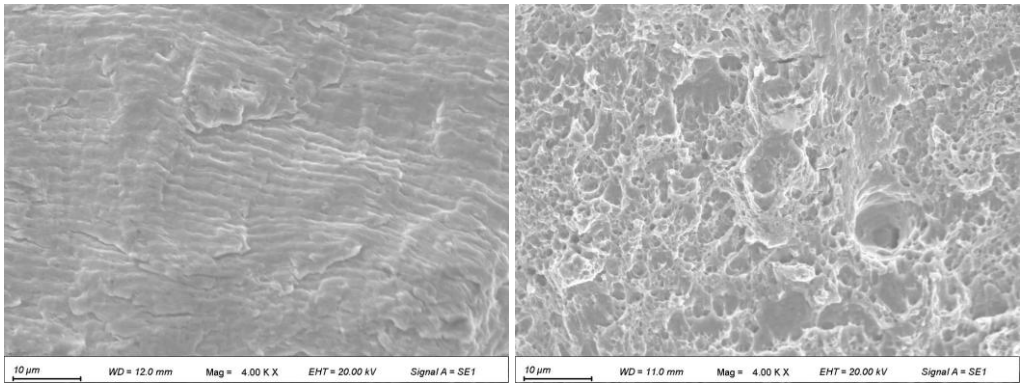


(c) Crack propagation region (d) Final fracture region

Fig. 6 Fracture morphology of a long-life HCF specimen at R = −1

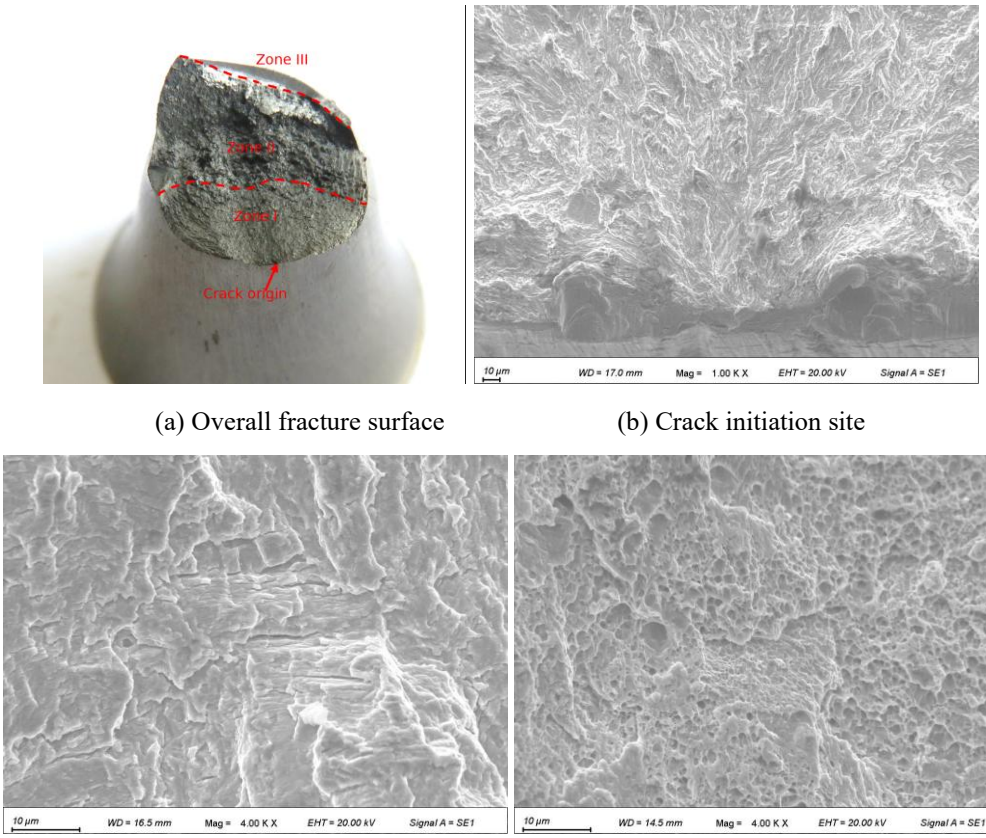


(a) Overall fracture surface (b) Crack initiation site



(c) Crack propagation region (d) Final fracture region

Fig. 7 Fracture morphology of a long-life HCF specimen at R = −0.5



(a) Overall fracture surface (b) Crack initiation site

(c) Crack propagation region (d) Final fracture region

Fig. 8 Fracture morphology of a long-life HCF specimen at R = 0.1

3.4. Fatigue Crack Growth in Different Joint Regions at 450 °C

Figures 9–12 show the da/dN–ΔK curves at 450 °C for the root weld metal, near-outer-surface weld metal, and right and left HAZs at the three stress ratios. Within the stable crack-growth regime, the curves were approximately linear on logarithmic axes, showing that the Paris power law adequately represents the measured FCG rates over the fitted intervals. The individual fitted C and m values for all 24 CT specimens appear in Table 5.

$$da/dN = C(\Delta K)^m \quad (3)$$

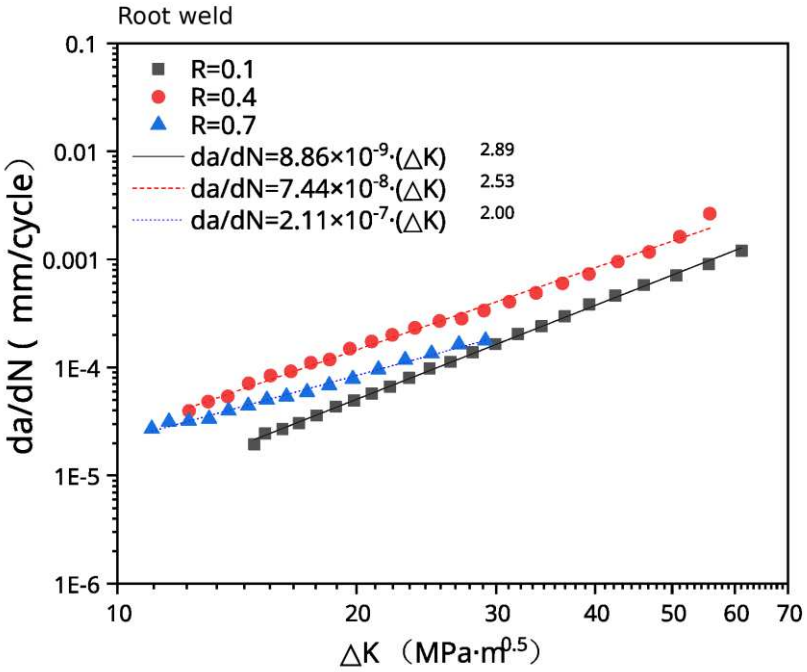


Fig. 9 Fatigue crack growth rates in the root weld metal at different stress ratios

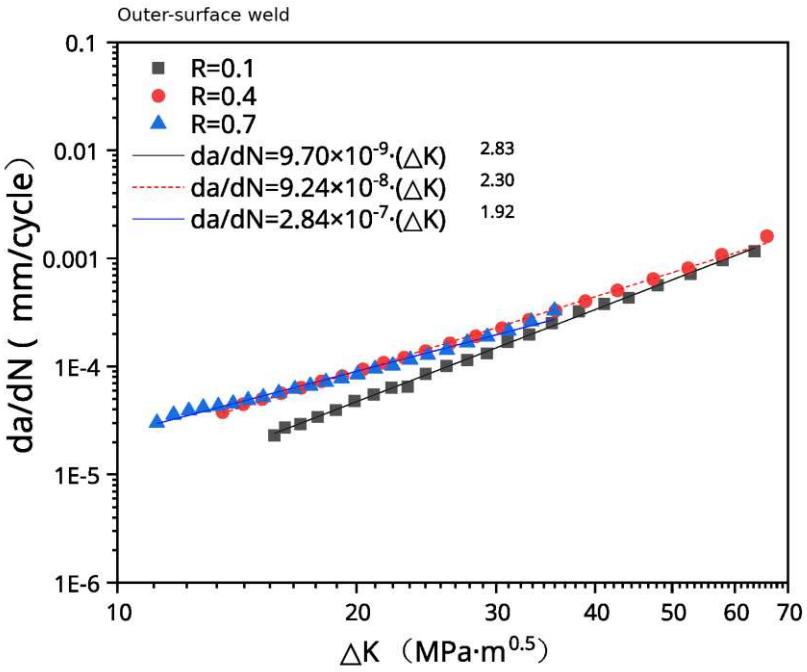


Fig. 10 Fatigue crack growth rates in the near-outer-surface weld metal at different stress ratios

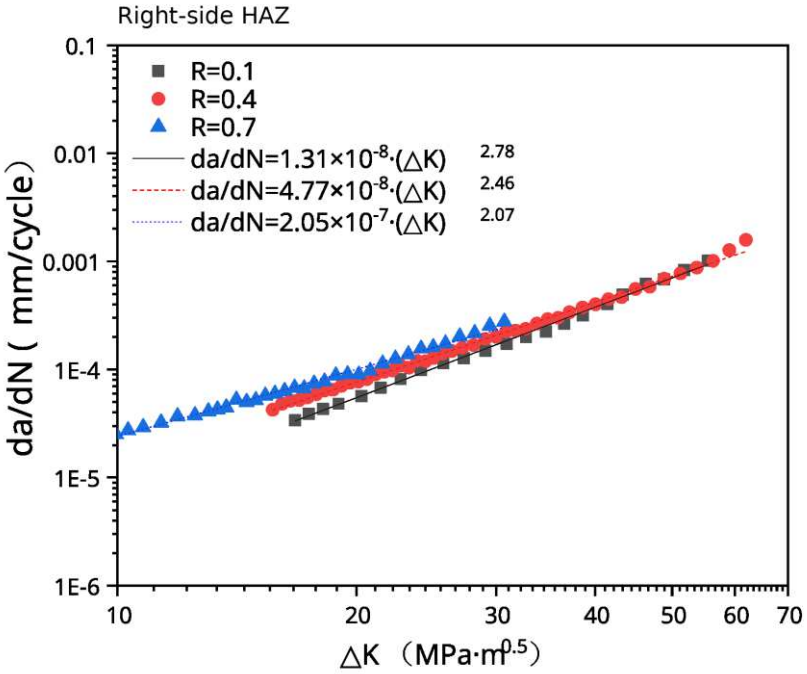


Fig. 11 Fatigue crack growth rates in the right HAZ at different stress ratios

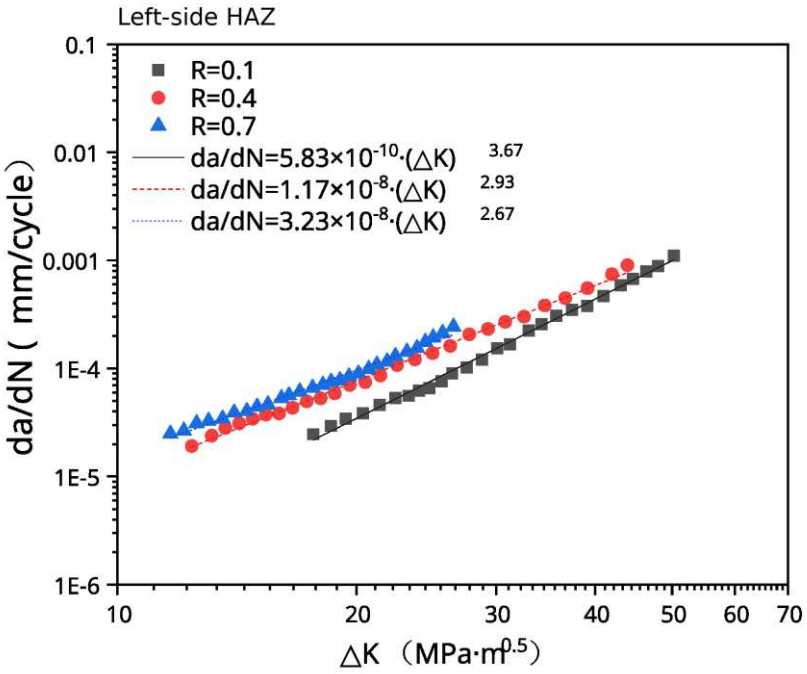


Fig. 12 Fatigue crack growth rates in the left HAZ at different stress ratios

The Paris parameters depended on specimen location and stress ratio and also varied between paired specimens tested under the same conditions. For the left HAZ at R = 0.1, the two m values were 3.746 and 3.668, whereas the corresponding values for the root weld metal at R = 0.7 were 2.324 and 1.999. These differences identify variations in the slopes of the fitted FCG curves among locations and loading conditions.

Table 5. Individual Paris-law parameters for the 24 CT specimens tested at 450 °C

Region	R	CT specimen ID	C	m
Root weld metal	0.1	B2-H-K-GH-010	4.845e-09	3.025

Region	R	CT specimen ID	C	m
Root weld metal	0.1	B2-H-K-GH-012	8.866e-09	2.888
Root weld metal	0.4	B2-H-K-GH-004	6.760e-08	2.391
Root weld metal	0.4	B2-H-K-GH-011	7.448e-08	2.529
Root weld metal	0.7	B2-H-K-GH-005	9.726e-08	2.324
Root weld metal	0.7	B2-H-K-GH-006	2.110e-07	1.999
Near-outer-surface weld metal	0.1	B2-H-K-WH-005	2.424e-08	2.599
Near-outer-surface weld metal	0.1	B2-H-K-WH-006	9.690e-09	2.834
Near-outer-surface weld metal	0.4	B2-H-K-WH-010	9.249e-08	2.297
Near-outer-surface weld metal	0.4	B2-H-K-WH-012	6.521e-08	2.412
Near-outer-surface weld metal	0.7	B2-H-K-WH-004	2.843e-07	1.922
Near-outer-surface weld metal	0.7	B2-H-K-WH-011	2.070e-07	2.052
Left HAZ	0.1	B2-H-K-WL-010	4.863e-10	3.746
Left HAZ	0.1	B2-H-K-WL-012	5.829e-10	3.668
Left HAZ	0.4	B2-H-K-WL-005	1.167e-08	2.934
Left HAZ	0.4	B2-H-K-WL-006	5.799e-09	3.182
Left HAZ	0.7	B2-H-K-WL-004	6.078e-08	2.469
Left HAZ	0.7	B2-H-K-WL-011	3.225e-08	2.672
Right HAZ	0.1	B2-H-K-WR-010	1.702e-08	2.720
Right HAZ	0.1	B2-H-K-WR-012	1.279e-08	2.791
Right HAZ	0.4	B2-H-K-WR-004	3.934e-08	2.511
Right HAZ	0.4	B2-H-K-WR-011	4.782e-08	2.462
Right HAZ	0.7	B2-H-K-WR-005	2.059e-07	2.066
Right HAZ	0.7	B2-H-K-WR-006	1.590e-07	2.149

For all four regions, the stable crack-growth rate increased with ΔK, but the differences among the curves involved more than parallel shifts. For example, the two root-weld specimens tested at R = 0.4 had m values of 2.391 and 2.529, whereas the corresponding values for the left HAZ at R = 0.1 were 3.746 and 3.668. Changes in the Paris exponent altered the relative growth rates as ΔK increased, and comparison of the fitted da/dN values at a common ΔK offered a more direct measure of the relative growth response.

3.5. Effect of Stress Ratio on FCG in Different Joint Regions

The two-specimen mean fitted rate for the root weld metal did not increase monotonically with stress ratio. At $\Delta K = 20$ MPa·m$^{1/2}$, the rates were 4.62×10^{-5}, 1.16×10^{-4}, and 9.34×10^{-5} mm/cycle for R = 0.1, 0.4, and 0.7, respectively. At $\Delta K = 25$ MPa·m$^{1/2}$, they were 8.93×10^{-5}, 2.02×10^{-4}, and 1.52×10^{-4} mm/cycle. The mean rate at R = 0.4 was approximately 25% and 33% higher than that at R = 0.7 at the two ΔK levels, respectively.

In the near-outer-surface weld metal, the rates at R = 0.4 and R = 0.7 were comparable. At $\Delta K = 20$ MPa·m$^{1/2}$, their mean fitted values were 8.98×10^{-5} and 9.34×10^{-5} mm/cycle, respectively; at $\Delta K = 25$ MPa·m$^{1/2}$, the corresponding values were 1.52×10^{-4} and 1.46×10^{-4} mm/cycle. In contrast, the mean rates in both HAZs generally increased with R at the two selected ΔK levels. The stress-ratio dependence of FCG rate therefore differed among the investigated regions.

The root weld metal, near-outer-surface weld metal, and both HAZs responded differently to stress ratio. The mean growth rates in the HAZs typically increased with R, whereas the magnitude of the rate change and the relative positions of the weld-metal curves depended on ΔK.

3.6. Comparison of FCG Rates at Common ΔK Values

The individual Paris fits of the 24 CT specimens provided fitted FCG rates at $\Delta K = 20$ and 25 MPa·m$^{1/2}$ within the common fitted intervals. Table 6 reports the two-specimen mean fitted rate and relative difference D for each region–stress-ratio combination.

Table 6. Mean fitted FCG rates and relative differences between paired CT specimens at common ΔK values

Region	R	da/dN at ΔK = 20	D20 (%)	da/dN at ΔK = 25	D25 (%)
Root weld metal	0.1	4.624e-05	19.3	8.932e-05	16.3
Root weld metal	0.4	1.163e-04	50.0	2.021e-04	52.8
Root weld metal	0.7	9.342e-05	19.8	1.520e-04	27.0
Near-outer-surface weld metal	0.1	5.274e-05	21.2	9.646e-05	16.0
Near-outer-surface weld metal	0.4	8.984e-05	0.5	1.519e-04	2.1
Near-outer-surface weld metal	0.7	9.339e-05	7.2	1.456e-04	10.1
Right HAZ	0.1	5.678e-05	7.3	1.050e-04	5.7
Right HAZ	0.4	7.454e-05	4.8	1.298e-04	3.7
Right HAZ	0.7	9.987e-05	1.0	1.598e-04	0.9
Left HAZ	0.1	3.543e-05	5.2	8.104e-05	7.0
Left HAZ	0.4	7.832e-05	4.4	1.551e-04	9.9
Left HAZ	0.7	9.783e-05	2.6	1.736e-04	2.0

At $\Delta K = 20$ MPa·m$^{1/2}$ and R = 0.1, the mean fitted FCG rate in the left HAZ was 3.54×10^{-5} mm/cycle, 37.6% below the value of 5.68×10^{-5} mm/cycle in the right HAZ. At R = 0.4, the mean rate in the root weld metal reached 1.16×10^{-4} mm/cycle, exceeding the values of 7.45×10^{-5}–8.98×10^{-5} mm/cycle in the near-outer-surface weld metal and both HAZs. These comparisons indicate that the relative FCG behavior of the joint regions changes with stress ratio.

At $\Delta K = 25$ MPa·m$^{1/2}$ and R = 0.1, the mean rates were 1.05×10^{-4} mm/cycle in the right HAZ and 8.10×10^{-5} mm/cycle in the left HAZ. At R = 0.7, the left HAZ showed the highest mean rate among the four regions, at 1.74×10^{-4} mm/cycle, compared with 1.52×10^{-4} mm/cycle in the root weld metal. Together, the two ΔK comparisons show that the relative FCG resistance of the sampled regions varies with both stress ratio and crack-driving-force level.

The paired-specimen results showed marked differences in repeatability among loading conditions and locations. In the near-outer-surface weld metal at R = 0.4, D was only 0.5% and 2.1% at $\Delta K = 20$ and 25 MPa·m$^{1/2}$, respectively, whereas the corresponding values in the root weld metal were 50.0% and 52.8%. The larger scatter in the root weld metal at this stress ratio contrasts with the smaller differences observed for most HAZ combinations and demonstrates region- and loading-condition-dependent interspecimen variability.

3.7. Characterization of Stress-Ratio Effects Using the Walker Model

Data obtained at multiple stress ratios were fitted separately for each joint region using ΔK, Kmax, and the Walker-corrected driving-force formulation. Corresponding coefficients of determination and Walker parameters are reported in Table 7.

Table 7. Results of combined fitting using different crack-driving-force formulations

Region	ΔK-based R^2	Kmax-based R^2	Walker R^2	Walker γ
Root weld metal	0.869	0.434	0.895	0.819
Near-outer-surface weld metal	0.928	0.454	0.965	0.806
Right HAZ	0.953	0.439	0.989	0.792
Left HAZ	0.890	0.328	0.971	0.753

With ΔK as the sole driving-force parameter, the combined fits for the four regions yielded R^2 values of 0.869–0.953. Using Kmax reduced these values to 0.328–0.454. The Walker correction raised R^2 to 0.895–0.989; the values for the right and left HAZs reached 0.989 and 0.971, respectively. Of the three formulations evaluated on the same data, the Walker form provided the highest goodness of fit for the combined multi-stress-ratio datasets.

Fitted Walker parameter γ ranged from 0.753 to 0.819 across the four regions. The root weld metal had γ = 0.819 with R^2 = 0.895, whereas the right HAZ had γ = 0.792 with R^2 = 0.989. Variations in the fitted parameter values and goodness of fit reflect the region-dependent response of the welded joint to changes in stress ratio.

4. Discussion

4.1. Mean-Stress Effect on High-Cycle Fatigue

Comparing HCF strength across stress ratios requires distinguishing between maximum stress and cyclic stress amplitude. For example, as R increased from −1 to 0.1, the 10^7-cycle conditional fatigue strength expressed as maximum stress increased from 300 to 550 MPa. Over the same range, the corresponding stress amplitude decreased from 300.0 to 247.5 MPa, while the tensile mean stress increased from 0 to 302.5 MPa. Comparable trends were observed in the constant-life stress-amplitude–mean-stress relationships at other fatigue lives. These results demonstrate that an increase in tensile mean stress reduces the allowable cyclic stress amplitude of the welded joint.

The strength measured at 10^7 cycles represents a conditional value tied to the specified run-out limit. Considered together with the constant-life relationships at 10^5 and 10^6 cycles, the data show a mean-stress effect throughout the investigated HCF life range, rather than only near run-out. Expressing fatigue conditions by the pair (σ_a, σ_m), instead of maximum stress σ_{max} alone, captures the combined change in cyclic amplitude and mean stress as R varies in this dissimilar-steel welded rotor joint.

4.2. Crack Initiation and Fracture Morphology under HCF Loading

Crack initiation locations differed among the representative fracture surfaces. Some specimens initiated near the free surface; others had initiation sites adjacent to subsurface cavities or Al–O-rich particles. Several initiation sites were evident in the short-life specimen tested at R = 0.1, consistent with the role of local discontinuities and particle distributions in initiation. In Fig. 4, an Al–O-rich particle lies close to a subsurface origin, suggesting that such local heterogeneities may provide favorable sites for fatigue crack initiation.

4.3. Region-Dependent FCG Behavior at 450 °C

All four regions followed Paris-type behavior in the stable growth regime at 450 °C, but the curves differed in both position and slope. At ΔK = 20 MPa·m$^{1/2}$, the mean rate in the left HAZ was lower than that in the right HAZ at R = 0.1; the root weld metal had the highest mean rate at R = 0.4; and the rates of the four regions became more similar at R = 0.7. Thus, no single region maintained a fixed ranking in FCG rate across the tested stress ratios and crack-driving-force levels. Previous studies on 9Cr/CrMoV joints [3], Ni-Cr-Mo-V weld metal [13], and ex-service CrMoV welds [14] have likewise documented associations between weld regions and FCG behavior in their respective material systems.

At a given R and ΔK, the fitted FCG rate depends jointly on the Paris coefficient C and exponent m. Differences in these parameters alter the relative rates among regions as ΔK changes. At R = 0.7 and ΔK = 25 MPa·m$^{1/2}$, for example, the mean rate in the left HAZ was 1.74×10^{-4} mm/cycle, compared with 1.52×10^{-4} mm/cycle in the root weld metal; at R = 0.4, the root weld metal exhibited a higher mean rate than either HAZ. These comparisons show that region-to-region differences in FCG behavior are dependent on stress ratio and ΔK.

Paired-specimen analysis also revealed differences in FCG behavior within nominally identical region–loading combinations. At R = 0.4, the relative differences between the two root-weld specimens were 50.0% and 52.8% at ΔK = 20 and 25 MPa·m$^{1/2}$, respectively, whereas the corresponding differences in the near-outer-surface weld metal were only 0.5% and 2.1%. The contrast shows that the extent of interspecimen scatter differs substantially among weld locations, even at the same nominal stress ratio.

4.4. Region Dependence of the Stress-Ratio Effect

The response to stress ratio varied considerably across joint regions. In the root weld metal, the two-specimen mean fitted rates at R = 0.4 were approximately 25% and 33% higher than those at R = 0.7 at ΔK = 20 and 25 MPa·m$^{1/2}$, respectively; in the near-outer-surface weld metal, the two stress-ratio groups had similar rates. In contrast, the mean rates in both HAZs generally increased with R, showing a more consistent nominal stress-ratio dependence.

The differing responses of the weld metals and HAZs show that increasing the nominal stress ratio does not necessarily produce the same displacement of FCG curves in every part of a welded joint. Previous investigations of

welded structures have investigated residual stress and effective stress ratio on crack growth [10–12], while near-threshold studies of heat-resistant steel welds have also demonstrated stress-ratio sensitivity [5,6]. The region-dependent response and non-monotonic mean-rate trend observed here in the Paris regime illustrate the spatial heterogeneity of stress-ratio effects in dissimilar-steel welded joints.

4.5. Effect of the Walker Stress-Ratio Correction

At fixed R, Paris relationships described the stable FCG rates, whereas curves obtained at different R values for the same region showed relative shifts. Incorporation of the stress-ratio term through the Walker relationship improved the R^2 of the combined fits for all four regions. The improvement is consistent with the empirical stress-ratio correction proposed by Walker [7]. Related modeling has been applied to welded joints in EH690 high-strength marine steel [15], although the materials and loading conditions differ.

Walker correction performance varied among regions. The combined-fit R^2 was 0.989 in the right HAZ but only 0.895 in the root weld metal, with fitted γ values ranging from 0.753 to 0.819. Compared with the more regular stress-ratio trends in the HAZs, the non-monotonic mean-rate response of the root weld metal under certain conditions was less readily collapsed by a single correction. Although the Walker approach improved the overall empirical fits, regional differences remained evident in the optimum parameters and fit residuals.

Region-specific Paris relationships describe local crack growth in the dissimilar-steel joint, while Walker correction provides a combined representation of stress-ratio dependence within each region at 450 °C. Used together, the two approaches distinguish regional growth behavior from the variation associated with stress ratio.

5. Conclusions

(1) At R = −1, −0.5, and 0.1, the conditional fatigue strengths at 10^7 cycles at room temperature were 300, 383, and 550 MPa, respectively, expressed as maximum stress. The corresponding stress amplitudes were 300.0, 287.5, and 247.5 MPa. Increasing tensile mean stress from 0 to 302.5 MPa lowered the allowable amplitude by 17.5%, with similar trends in constant-life relationships at 10^5 and 10^6 cycles.

(2) Representative HCF fracture surfaces showed distinct crack initiation, stable propagation, and final fracture regions. Fatigue striations and localized quasi-cleavage-like features occurred in the propagation regions, whereas dimples predominated in the final fracture regions. Cracks initiated at surface or subsurface discontinuities, and Al–O-rich particles were found near some subsurface initiation sites.

(3) Paris relationships described stable FCG data from all 24 CT specimens at 450 °C. At a common ΔK, growth rates differed among the four joint regions and their relative ranking varied with R and ΔK. At $\Delta K = 20$ MPa·m$^{1/2}$ and R = 0.1, the two-specimen mean fitted rate in the left HAZ was 37.6% lower than that in the right HAZ.

(4) In the root weld metal, the mean fitted rates at R = 0.4 were approximately 25% and 33% higher than those at R = 0.7 at $\Delta K = 20$ and 25 MPa·m$^{1/2}$, respectively, indicating a non-monotonic stress-ratio trend in the group means. The paired-specimen relative differences at R = 0.4 were 50.0% and 52.8%, respectively. In contrast, the mean rates in both HAZs generally increased with R at these ΔK levels.

(5) The Walker correction raised the combined-fit R^2 for the four regions from 0.869–0.953 with ΔK alone to 0.895–0.989, with optimal γ values ranging from 0.753 to 0.819. Differences in fitted parameters and the extent of improvement among regions reflect the regional dependence of the stress-ratio effect.

References

[1] W.K. Wang, Z.Z. Xu, B. Zhu, et al., Mater. Res. Express 7, 016565 (2020). https://doi.org/10.1088/2053-1591/ab66aa

[2] W.K. Wang, Y. Liu, Y. Guo, et al., Mater. Sci. Eng. A 786, 139473 (2020). https://doi.org/10.1016/j.msea.2020.139473

[3] X.L. Deng, F.G. Lu, H.C. Cui, et al., Mater. Sci. Eng. A 651, 1018–1030 (2016). https://doi.org/10.1016/j.msea.2015.11.081

[4] Q. Wang, M. Liu, Y. Cai, et al., Int. J. Fatigue 170, 107534 (2023). https://doi.org/10.1016/j.ijfatigue.2023.107534

[5] Q. Sun, K. Li, X. Li, et al., Int. J. Fatigue 137, 105650 (2020). https://doi.org/10.1016/j.ijfatigue.2020.105650

[6] Q. Sun, Q. Liu, X. Li, et al., Int. J. Fatigue 164, 107175 (2022). https://doi.org/10.1016/j.ijfatigue.2022.107175

[7] K. Walker, The effect of stress ratio during crack propagation and fatigue for 2024-T3 and 7075-T6 aluminum, in Effects of Environment and Complex Load History on Fatigue Life, ASTM STP 462 (ASTM International, 1970), pp. 1–14. https://doi.org/10.1520/STP32032S

[8] GB/T 3075–2021, Metallic materials—Fatigue testing—Axial force-controlled method (National Standard of the People's Republic of China, 2021)

[9] GB/T 6398–2017, Metallic materials—Fatigue testing—Fatigue crack growth method (National Standard of the People's Republic of China, 2017)

[10] Y. Xu, R. Bao, H. Liu, et al., Fatigue Fract. Eng. Mater. Struct. 40, 1227–1239 (2017). https://doi.org/10.1111/ffe.12617

[11] Q. Wang, Z.J. Yan, X.S. Liu, et al., Eng. Fract. Mech. 194, 224–239 (2018). https://doi.org/10.1016/j.engfracmech.2018.03.016

[12] L. Bercelli, B. Levieil, C. Doudard, et al., Eng. Fract. Mech. 279, 109061 (2023). https://doi.org/10.1016/j.engfracmech.2023.109061

[13] C. Han, Q. Liu, Z. Cai, et al., Int. J. Fatigue 176, 107859 (2023). https://doi.org/10.1016/j.ijfatigue.2023.107859

[14] Q. Sun, X. Li, K. Li, et al., Int. J. Fatigue 152, 106460 (2021). https://doi.org/10.1016/j.ijfatigue.2021.106460

[15] X. Shen, X. Gao, Y. Shao, et al., Int. J. Fatigue 189, 108572 (2024). https://doi.org/10.1016/j.ijfatigue.2024.108572